

Multiscale analysis of the CMB temperature derivatives

A. Marcos-Caballero,^{a,b} E. Martínez-González^a and P. Vielva^a

^aInstituto de Física de Cantabria, CSIC-Universidad de Cantabria,
Avda. de los Castros s/n, 39005 Santander, Spain.

^bDpto. de Física Moderna, Universidad de Cantabria,
Avda. los Castros s/n, 39005 Santander, Spain.

E-mail: marcos@ifca.unican.es, martinez@ifca.unican.es, vielva@ifca.unican.es

Abstract. We study the Planck CMB temperature at different scales through its derivatives up to second order, which allows one to characterize the local shape and isotropy of the field. The problem of having an incomplete sky in the calculation and statistical characterization of the derivatives is addressed in the paper. The analysis confirms the existence of a low variance in the CMB at large scales, which is also noticeable in the derivatives. Moreover, deviations from the standard model in the gradient, curvature and the eccentricity tensor are studied in terms of extreme values on the data. As it is expected, the Cold Spot is detected as one of the most prominent peaks in terms of curvature, but additionally, when the information of the temperature and its Laplacian are combined, another feature with similar probability at the scale of 10° is also observed. However, the p -value of these two deviations increase above the 6% when they are referred to the variance calculated from the theoretical fiducial model, indicating that these deviations can be associated to the low variance anomaly. Finally, an estimator of the directional anisotropy for spinorial quantities is introduced, which is applied to the spinors derived from the field derivatives. An anisotropic direction whose probability is $< 1\%$ is detected in the eccentricity tensor.

Contents

1	Introduction	1
2	Theoretical framework	2
3	Data processing	3
4	Pixel covariance in the presence of a mask	5
5	Covariance of the derivatives	6
6	Extreme deviations in the derivatives fields	9
7	Directional analysis	11
8	Conclusions	15
A	Integrals of the spin-weighted spherical harmonics	17

1 Introduction

In the standard cosmological model, the high level of isotropy of the Cosmic Microwave Background (CMB) observations are explained by evoking a phase of exponential expansion in the early Universe, called cosmic inflation. Following the standard predictions of inflation, the initial perturbations are Gaussianly distributed in a homogeneous flat space. Deviations in the isotropy and Gaussianity of the CMB temperature field are important to constrain the particular model of inflation, or even to explore new physics in the primordial Universe.

Although the recent measurements of the CMB have a good agreement with the concordance model of cosmology [1], there exists evidences of particular deviations from the isotropy assumption as the dipole modulation [2, 3], parity violation asymmetry [4–6] or the quadrupole and octopole alignment [7]. Additionally, there are indications that the CMB temperature presents a low variance [8] and a lack of correlation [9, 10] at large scales. Moreover, the Cold Spot anomaly [11, 12] is characterized as an extreme on a particular wavelet scale located in a specific region of the sky which presents a deviation from Gaussianity. All these anomalies have the common property that are especially dominated by the large scale behaviour of the CMB.

The analysis of the temperature gradient and higher order derivatives are useful for the characterization of the CMB anisotropies. For instance, at small scales, the temperature gradient have been used to reconstruct the matter density power spectrum using the gravitational lensing effect over the CMB photons [13], as well as to study the beam asymmetry systematic introduced by the scanning strategy [14]. In a recent paper, the shape of the large-scale peaks are analysed by considering the value of the Laplacian and the eccentricity tensor at the centre of the peak [15]. In this work, we are interested in the large scale behaviour of the CMB temperature derivatives, for which different scales are analysed. If the scaling function is a Gaussian filter, the multiscale analysis based on the scalar curvature (the Laplacian) is equivalent to the Spherical Mexican Hat Wavelet [11, 16]. On the other hand,

the spinorial derivatives (the gradient and the eccentricity tensor) have information about the local directionality of the CMB temperature, which have been studied previously by using the steerable wavelets formalism [17–19]. We present here a joint analysis of the derivatives field for a wide range of scales (from 1° to 30°), paying attention to the extreme deviations with respect to the standard model expectation.

The scalar curvature, as well as the temperature itself, allow one to analyse the CMB in terms of rotational invariant quantities, which, in particular, characterizes Cold Spot-like features on the sky. Besides the scalar derivatives, the modulus of the gradient and the eccentricity tensor can be studied in order to localize regions on the sky with anomalous dipolar or quadrupolar local shape. Moreover, due to the directional character of these derivatives, the gradient and the eccentricity tensor can be also used to measure the isotropy of the field. For this purpose, an estimator for spinorial quantities based on the geodesic projection on a particular direction on the sphere is introduced.

This paper is organised as follows: in Section 2, the calculation of the field derivatives in terms of the spherical harmonic coefficients is introduced, whereas the data processing is described in Section 3. A new formalism regarding the statistics of the derivative fields in the presence of a mask is introduced in Section 4. The first analysis of this work is performed in Section 5, which consists in the calculation and study of the covariance of the different derivatives components. On the other hand, extreme values of the derivative fields are analysed and compared with the standard model prediction in Section 6. In addition, the directional analysis of the spinorial derivatives is considered in Section 7, in order to quantify the isotropy of the CMB temperature field. Finally, the conclusions of the paper are exposed in Section 8.

2 Theoretical framework

A field on the sphere is commonly described by the spherical coordinates, and consequently, its derivatives are taken along the directions determined by the local basis vectors \mathbf{e}_θ and \mathbf{e}_ϕ . Additionally, it is useful to coordinate the tangent plane in terms of the helicity basis $\mathbf{e}_\pm = \mathbf{e}_\theta \pm i\mathbf{e}_\phi$, particularly when the derivatives are expressed in the spherical harmonic space. The reason for using this system of reference is that the covariant derivatives in the helicity basis modify the spherical harmonics as the spin raising/lowering operators, which simplifies the calculations. This implies, in particular, that the derivatives of a field on the sphere can be spanned in terms of the spin-weighted spherical harmonics, whose spin depends on which type of derivative is considered. Since spinors with different rank are statistically independent, we classify the derivatives up to second order in two scalars ($s = 0$), one vector ($s = 1$) and one tensor ($s = 2$), which allows to make an independent analysis for each spin. The scalar derivatives are the temperature field itself (zero-order derivative) and its Laplacian, which are mutually correlated, specially at large scales. On the other hand, the components of the gradient form a vector, while the local eccentricity is a 2-spin tensor determined by the second order derivatives. Following the notation in [20], the derivatives are given by

$$\nu_R(\mathbf{n}) = \frac{1}{\sigma_\nu(R)} \sum_{\ell=0}^{\infty} w_\ell(R) a_{\ell m} Y_{\ell m}(\mathbf{n}) , \quad (2.1a)$$

$$\kappa_R(\mathbf{n}) = \frac{1}{\sigma_\kappa(R)} \sum_{\ell=0}^{\infty} \frac{(\ell+1)!}{(\ell-1)!} w_\ell(R) a_{\ell m} Y_{\ell m}(\mathbf{n}) , \quad (2.1b)$$

$$\eta_R(\mathbf{n}) = \frac{1}{\sigma_\eta(R)} \sum_{\ell=1}^{\infty} \sqrt{\frac{(\ell+1)!}{(\ell-1)!}} w_\ell(R) a_{\ell m +1} Y_{\ell m}(\mathbf{n}) , \quad (2.1c)$$

$$\epsilon_R(\mathbf{n}) = \frac{1}{\sigma_\epsilon(R)} \sum_{\ell=2}^{\infty} \sqrt{\frac{(\ell+2)!}{(\ell-2)!}} w_\ell(R) a_{\ell m +2} Y_{\ell m}(\mathbf{n}) , \quad (2.1d)$$

where $w_\ell(R)$ represents the Fourier coefficients of the window function corresponding to a particular angular scale R (see Section 3 for the precise definition of this filter). In the equations above, the scalar quantities ν and κ are real fields, while the spinors η and ϵ are complex numbers, since they have a directional character. The corresponding complex conjugates are expressed in terms of the spherical harmonics with spin -1 and -2 , respectively. The derivatives in eqs. (2.1) are normalized by their corresponding theoretical variances, which are calculated assuming a fiducial model. They are expressed in terms of the angular power spectrum in the following way:

$$\sigma_\nu^2(R) = \sum_{\ell=0}^{\infty} \frac{2\ell+1}{4\pi} w_\ell^2(R) C_\ell , \quad (2.2a)$$

$$\sigma_\kappa^2(R) = \sum_{\ell=0}^{\infty} \frac{2\ell+1}{4\pi} \left[\frac{(\ell+1)!}{(\ell-1)!} \right]^2 w_\ell^2(R) C_\ell , \quad (2.2b)$$

$$\sigma_\eta^2(R) = \sum_{\ell=1}^{\infty} \frac{2\ell+1}{4\pi} \frac{(\ell+1)!}{(\ell-1)!} w_\ell^2(R) C_\ell , \quad (2.2c)$$

$$\sigma_\epsilon^2(R) = \sum_{\ell=2}^{\infty} \frac{2\ell+1}{4\pi} \frac{(\ell+2)!}{(\ell-2)!} w_\ell^2(R) C_\ell . \quad (2.2d)$$

The fact of normalizing the data by using a concrete theoretical model does not introduces a bias in the analysis, since it can be seen as a change of units in order to have unit variance quantities. The theoretical fiducial model assumed throughout the paper is $\Omega_b h^2 = 0.2222$, $\Omega_c h^2 = 0.1197$, $H_0 = 67.31$ km/s Mpc $^{-1}$, $\tau = 0.078$, $n_s = 0.9655$ and $\ln(10^{10} A_s) = 3.089$, which represent the Planck TT-lowP best-fit cosmological parameters ([1], table 3).

3 Data processing

The CMB temperature data analysed in the paper correspond to the cleaned maps delivered by the Planck collaboration. Since we are studying large scale structures, the foreground contamination may be important in the analysis and could introduce spurious signals. For this reason, two of the four official temperature maps provided by Planck are considered, namely, SEVEM and SMICA [21]. These two maps are given in the Healpix pixelation scheme with resolution $N_{\text{side}} = 2048$ [22], and filtered by a Gaussian beam whose FWHM is $5'$ and the corresponding pixel window function. In terms of the spherical harmonic coefficients, these maps have a band limit of $\ell_{\text{max}} = 4000$.

In order to consider CMB anisotropies at different scales, the maps are filtered by a Gaussian function. The corresponding filter on the sphere is obtained from the stereographic projection of the two-dimensional Euclidean Gaussian distribution, whose Fourier coefficients are given by:

$$w_\ell(R) = \exp \left[-\frac{\ell(\ell+1)}{2R^2} \right] , \quad (3.1)$$

id	R [deg]	N_{side}	ℓ_{max}
1	1.00	256	767
2	1.20	256	767
3	1.43	256	767
4	1.71	256	767
5	2.04	128	383
6	2.44	128	383
7	2.92	128	383
8	3.49	128	383
9	4.17	64	191
10	4.99	64	191

id	R [deg]	N_{side}	ℓ_{max}
11	5.96	64	191
12	7.13	64	191
13	8.53	32	95
14	10.21	32	95
15	12.22	32	95
16	14.65	32	95
17	17.57	16	47
18	21.11	16	47
19	25.42	16	47
20	30.71	16	47

Table 1. Different scales considered in the paper. The first column indicates the labels used in Figure 6 to refer to that scale. The second column is the angular scale size R measured in degrees. Finally, the third and fourth columns represent the resolution (N_{side}) and the band limit (ℓ_{max}) used in the calculations of that particular scale, respectively.

where the scale R , characterizing the width of the filter, represents the standard deviation of a two-dimensional Gaussian function in the Euclidean space. The linear scale R is related to the angular size θ on the sphere by $R = 2 \tan \frac{\theta}{2}$. However, the difference between these two quantities is only important at large scales. Throughout the paper, twenty angular scales from 1° to 30° , which are chosen with logarithmic steps, are considered in the analysis (see table 1).

The data maps at the different scales are calculated by performing the spherical harmonic transform of the temperature field up to the given multipole and applying the filter $w_\ell(R)$ for each scale. Before calculating the spherical harmonic coefficients, the maps are masked with their respective confidence masks, and subsequently, the monopole and dipole are removed in the remaining area. In this procedure, the maps are deconvolved in order to remove the effective beam and pixel window function present initially in the data. The derivative fields are computed from the spherical harmonic coefficients following eqs. (2.1a-2.1d). The resulting maps are generated again in the Healpix pixelisation scheme whose resolution depends on the scale R considered. This optimal resolution (in the sense of working at the lowest resolution that retains all the useful information of the filtered signal) is defined by taking into account the properties of the stereographic projection:

$$N_{\text{side}} \gtrsim \sqrt{\frac{1}{12} \left(1 + \frac{4N}{R^2} \right)}, \quad (3.2)$$

where N represents the number of pixels in the area defined by a circle of radius R . Since the values of N_{side} are only powers of 2, the Healpix resolution whose value is immediately greater than the right-hand-side of eq. (3.2) is taken. The gradient, the curvature and the eccentricity tensor require larger resolution than the temperature field, and, for this reason, the value of $N = 56$ is chosen, which we have tested that provides maps with the optimal resolution. Finally, the maps are generated considering only multipoles up to $\ell_{\text{max}} = 3N_{\text{side}} - 1$, once the corresponding pixel window function is applied. Of course, the same procedure is applied to the simulations used in the characterization of the statistical properties of the data.

4 Pixel covariance in the presence of a mask

Since we are considering a field smoothed at different scales, the mask applied to the data introduces different spurious correlations, and reduces the variance in the region close to it for each convolved version of the signal. In general, if the signal that we want to analyse presents correlations, the particular geometry of the mask becomes important and this effect is not trivial to consider analytically. For this reason, the systematics introduced by the mask are estimated by using a Monte Carlo methodology. Simulations of the CMB anisotropies are generated and masked accordingly to the observed sky in the data, and subsequently, the covariance of the derivatives at different scales are calculated in each pixel. Since the maps are smoothed after the mask is applied, the zeros imposed on unobserved pixels affects to the unmasked region depending on the size of the filter. For the largest scales considered in the paper, this effect may be especially important.

We have developed a formalism in which the effect of the mask in each pixel can be taken into account. The method is based on the decomposition of the covariance between different masked fields at each pixel as a linear transformation of the corresponding theoretical covariance obtained in the full-sky limit:

$$\hat{\mathbf{C}}(p) = \mathbf{R}(p) \mathbf{C} \mathbf{R}^t(p), \quad (4.1)$$

where $\hat{\mathbf{C}}(p)$ is the covariance in the pixel p for the masked map, \mathbf{C} is the full-sky covariance, which is independent of the map location, and $\mathbf{R}(p)$ is the transformation matrix relating them. As it is expected, this transformation depends on the sky location due to the anisotropy introduced by the mask. Since the mask geometry can be complicated, the matrix $\mathbf{R}(p)$ is estimated by calculating simulations of the particular masked fields under consideration.

The matrix which defines the linear transformation in eq. (4.1) is unique, imposing the condition that it is lower triangular, in which case, it can be expressed as the product $\mathbf{R}(p) = \hat{\mathbf{L}}(p)\mathbf{L}^{-1}$, where $\hat{\mathbf{L}}(p)$ and \mathbf{L} are the lower triangular matrices obtained from the Cholesky decomposition of $\hat{\mathbf{C}}(p)$ and \mathbf{C} , respectively. In the particular case of two-dimensional covariances, the matrix $\mathbf{R}(p)$ is explicitly given by

$$\mathbf{R}(p) = \begin{pmatrix} \frac{\hat{\sigma}_1}{\sigma_1} & 0 \\ \frac{\hat{\sigma}_2}{\sigma_1} \left(\hat{\rho} - \rho \sqrt{\frac{1-\hat{\rho}^2}{1-\rho^2}} \right) & \frac{\hat{\sigma}_2}{\sigma_2} \sqrt{\frac{1-\hat{\rho}^2}{1-\rho^2}} \end{pmatrix}, \quad (4.2)$$

where σ_1 and σ_2 are the r.m.s. of the two considered random variables, and ρ is the correlation coefficient between them. The same quantities, but with the hat notation, indicates the corresponding variables when the field is masked. Notice that $\hat{\sigma}_1$, $\hat{\sigma}_2$ and $\hat{\rho}$ depend on the sky location due to the anisotropy introduced by the mask. Since the components of the matrix $\mathbf{R}(p)$ are formed by ratios of masked and unmasked quantities, it converges faster than $\hat{\mathbf{C}}(p)$ when they are estimated with simulations. For instance, for pixels away from the mask, where the effect of the smoothing on the derivatives is negligible, the matrix \mathbf{R} approaches to the identity with practically zero variance. On the other hand, if the covariance $\hat{\mathbf{C}}(p)$ is calculated directly, it is needed more simulations to converge with a desired precision, even in points for which the mask has no effect. For this reason, the covariance of the the masked fields $\hat{\mathbf{C}}(p)$ is calculated from eq. (4.1), where the transformation matrix $\mathbf{R}(p)$ is estimated with simulations and the full-sky covariance \mathbf{C} is computed theoretically.

Besides for the calculation of $\hat{\mathbf{C}}(p)$, the matrix $\mathbf{R}(p)$ in eq. (4.2) is used to construct an estimator of the one-point covariance of the derivative fields (see Section 5), and, additionally,

to take into account the observed low variance of the CMB [8] in the analysis performed in Sections 6 and 7.

5 Covariance of the derivatives

One of the anomalies in the CMB data is the low variance of the temperature field at large scales, which have been confirmed by several analyses [8, 23–25]. In this work, these studies are extended to the variance of each derivative field and the correlation between ν and κ . In order to take into account the smoothing effects on a incomplete sky, it is proposed an estimator that considers the different variance at each pixel. In particular, for two correlated variables given by the vector $\mathbf{x}(p) = (x_1(p), x_2(p))$, the estimator of their covariance matrix is

$$\begin{aligned} \mathbf{S}_{\mathbf{x}}^2 &= \frac{1}{N_{\text{pix}}} \sum_p \mathbf{R}^{-1}(p) \mathbf{x}(p) [\mathbf{R}^{-1}(p) \mathbf{x}(p)]^t = \\ &= \frac{1}{N_{\text{pix}}} \sum_p \mathbf{R}^{-1}(p) \begin{pmatrix} x_1^2(p) & x_1(p)x_2(p) \\ x_1(p)x_2(p) & x_2^2(p) \end{pmatrix} [\mathbf{R}^{-1}(p)]^t, \end{aligned} \quad (5.1)$$

where the anisotropy of the field due to the mask is considered by using the matrix $\mathbf{R}(p)$ defined in eq. (4.2) and N_{pix} represents to number of observed pixels. This expression is obtained by inverting eq. (4.1) to express the full-sky covariance as a function of the covariance from the data, which is estimated as the product of the two fields at each pixel, and averaging over the observed sky, once the correction given by the inverse of the matrix $\mathbf{R}(p)$ is applied. From eq. (5.1), it is possible to see that the estimator of the variance of the field x is

$$S_x^2 = \frac{\sigma_x^2}{N_{\text{pix}}} \sum_p \frac{|x(p)|^2}{\hat{\sigma}_x^2(p)}, \quad (5.2)$$

where we have included the modulus of x in order to generalize this expression for complex fields, like the gradient and the eccentricity tensor. These variances are calculated as a sum over all observed pixels weighted by the ratio $\sigma_x^2/\hat{\sigma}_x^2(p)$, which represents the anisotropy introduced by the mask. In the case of pixels away from the mask, the weights approach to unity, recovering the standard variance estimator for full sky maps. Averaging eq. (5.2), the variance of the field x is obtained, which implies that the estimator S_x^2 is unbiased.

In addition to the variances, the cross-correlation between the variables x and y can be calculated using the following estimator, which is obtained from the off-diagonal component of eq. (5.1):

$$S_{xy} = \frac{\sigma_x \sigma_y}{N_{\text{pix}}} \sum_p \frac{x(p)y(p)}{\hat{\sigma}_x(p)\hat{\sigma}_y(p)} \sqrt{\frac{1 - \rho^2}{1 - \hat{\rho}^2(p)}} + \frac{\sigma_x \sigma_y}{N_{\text{pix}}} \sum_p \frac{x^2(p)}{\hat{\sigma}_x^2(p)} \left(\rho - \hat{\rho}(p) \sqrt{\frac{1 - \rho^2}{1 - \hat{\rho}^2(p)}} \right). \quad (5.3)$$

The fact that the mask modifies the correlation coefficient of the two variables introduces a second term on the right-hand-side of this equation in order to prevent a biased estimation of the cross-correlation. In the particular case of having full-sky maps, S_{xy} coincides with the standard estimator of the cross-correlation of two variables.

In figure 1, it is represented the variance of the derivatives fields as a function of the scale. The variance of the normalized temperature field ν presents a low variance with significance greater than $2\text{-}\sigma$ for scales $> 2^\circ$. This result is in agreement with previous analyses of the

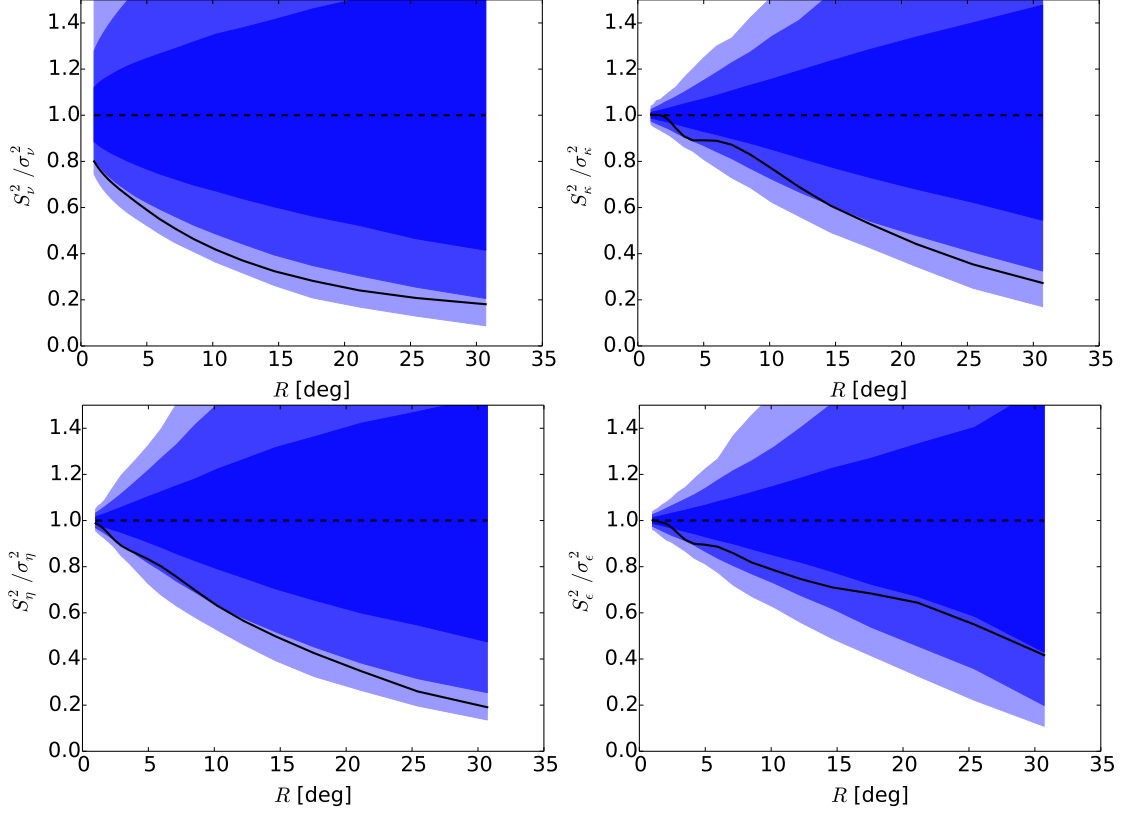


Figure 1. Variances of the derivatives fields ν , κ , η and ϵ as a function of the scale R , for the Planck SEVEM map. The three contours correspond to the one, two and three sigma regions.

low variance of the CMB temperature at large scales [25]. Regarding the derivatives, the gradient η and the curvature κ also have a low variance at large scale, which are significant for $R > 15^\circ$, whereas the eccentricity remains below the $2\text{-}\sigma$ level for all scales. Additionally, the low variance is also manifested in the cross-correlation of ν and κ for scales $R > 5^\circ$, but, on the other hand, this anomaly is no present in the cross-correlation coefficient, which is calculated normalizing by the observed standard deviations instead of their theoretical values (figure 2). This is an indication that, despite of low variance in ν and κ , the correlation of these two variables is compatible with the theoretical expectation. Both CMB Planck maps, SEVEM and SMICA, give similar results in terms of the variance of the derivative fields.

In addition to the analysis of the variance, it is possible to study the local isotropy of the field looking at the variance of the different components of the spinorial derivatives. Since the cosmological principle implies that any statistical quantity does not depend on the direction considered, the variance of each component must be the same as well as the correlation between them must vanish. In figure 3, the difference of the variances and the cross-correlation between the two components of η and ϵ are depicted, showing that the data are compatible with the isotropy of the field. Notice that these quantities depend on the particular choice of the coordinate system, indicating in this case, an alignment with the galactic north-south direction, which corresponds to the z -axis of the spherical coordinates. A more general analysis of the statistical isotropy of the derivatives, which is independent of the particular coordinate system assumed, is performed in Section 7.

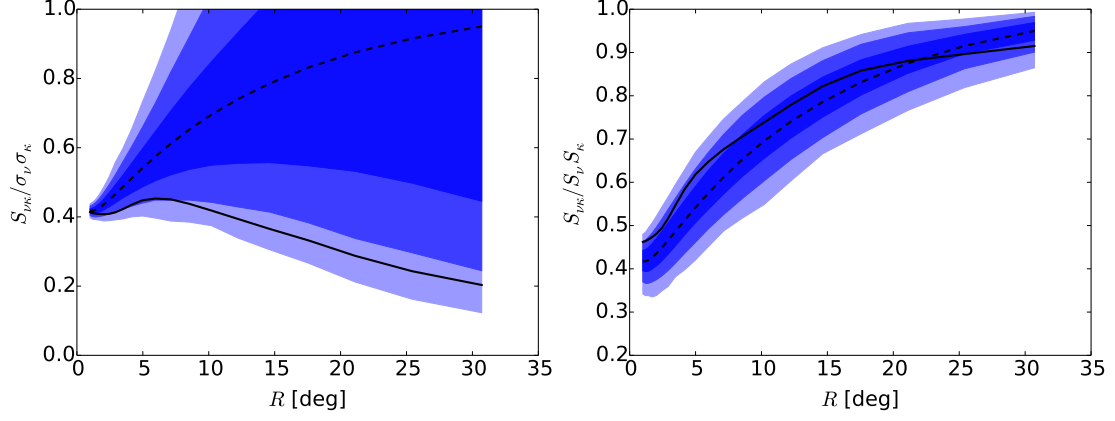


Figure 2. Cross-correlation $S_{\nu\kappa}$ between the temperature and the curvature (left), and its corresponding correlation coefficient (right) as a function of the scale, obtained from the Planck SEVEM map. The contours correspond to the one, two and three sigma regions.

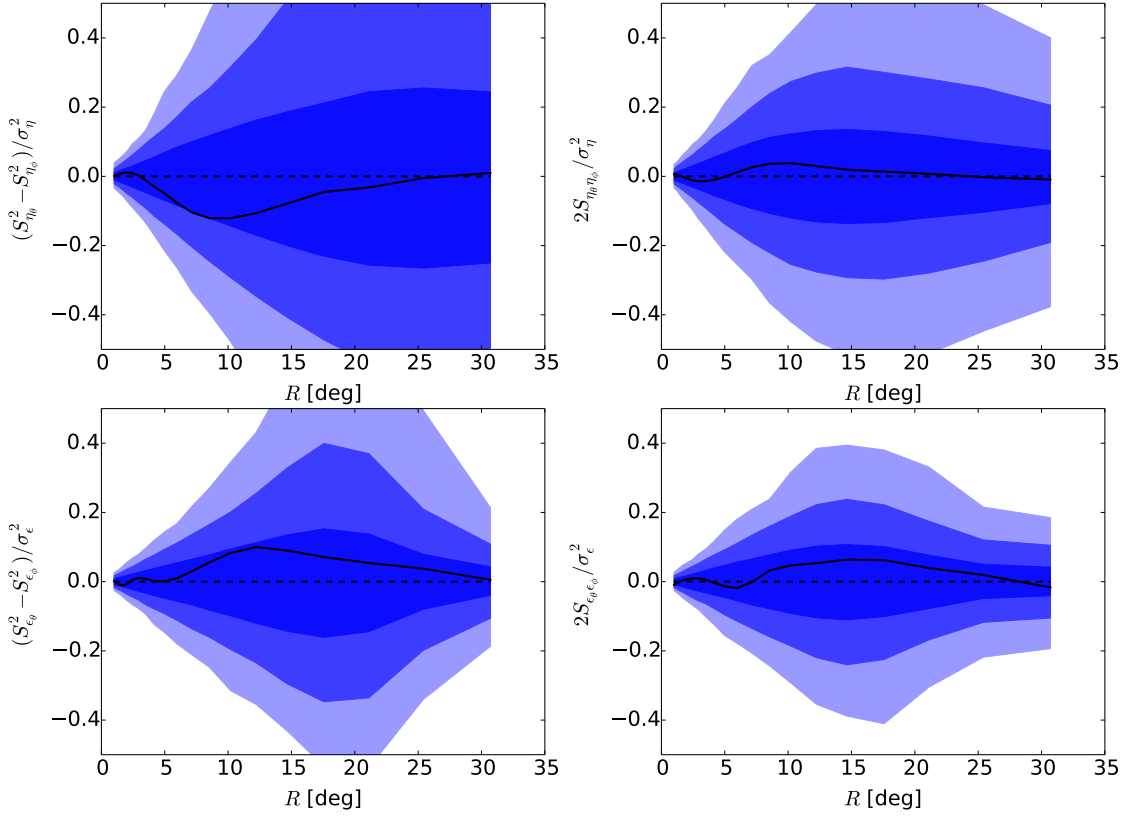


Figure 3. Difference of the variances (left) and cross-correlation (right) of the two component of the spinors η (upper row) and ϵ (bottom row). The curves are obtained from the Planck SEVEM data. The contours correspond to the one, two and three sigma regions.

6 Extreme deviations in the derivatives fields

In order to study deviations of the CMB temperature field and its derivatives from the standard model prediction, the tail probability of the one-point distribution for each pixel is calculated. Assuming the predictions of the simplest models of inflation, the CMB fluctuations are Gaussianly distributed and, therefore, the variables ν , κ and the components of the spinors η and ϵ are also Gaussian variables, since they are calculated applying linear operators over the CMB temperature field.

For the scalar degrees of freedom ν and κ , we define the following quantities:

$$\chi_\nu^2(p) = \frac{\nu^2(p)}{\hat{\sigma}_\nu^2(p)} \sigma_\nu^2, \quad (6.1a)$$

$$\chi_\kappa^2(p) = \frac{\kappa^2(p)}{\hat{\sigma}_\kappa^2(p)} \sigma_\kappa^2, \quad (6.1b)$$

$$\chi_s^2(p) = \mathbf{s}(p) \hat{\mathbf{C}}_s^{-1}(p) \mathbf{s}(p), \quad (6.1c)$$

where the vector $\mathbf{s} = (\nu, \kappa)$ is composed by the temperature and curvature fields, and $\hat{\mathbf{C}}_s(p)$ denotes the covariance of \mathbf{s} in the pixel p , which is calculated from eq. (4.1). If the temperature field is Gaussian, these quantities are distributed according to the χ^2 probability density. Whilst the χ^2 distribution has one degree of freedom in the case of χ_ν^2 and χ_κ^2 , the combination χ_s^2 has two degrees of freedom. In a similar way, it is computed the χ^2 quantities for the gradient and the eccentricity tensor:

$$\chi_\eta^2(p) = \boldsymbol{\eta}(p) \hat{\mathbf{C}}_\eta^{-1}(p) \boldsymbol{\eta}(p), \quad (6.2a)$$

$$\chi_\epsilon^2(p) = \boldsymbol{\epsilon}(p) \hat{\mathbf{C}}_\epsilon^{-1}(p) \boldsymbol{\epsilon}(p), \quad (6.2b)$$

where, in this case, the vectors $\boldsymbol{\eta}$ and $\boldsymbol{\epsilon}$ denote the components of the spinors η and ϵ , respectively.

In order to quantify deviations from the standard model, we compute the logarithm of the tail probability of χ^2 variables defined in eqs. (6.1-6.2):

$$r_x(p) = -\ln \text{P}\{\chi^2 > \chi_x^2(p)\}, \quad (6.3)$$

where x represents the field considered (ν , κ , s , η or ϵ). One advantage of this quantity is that it is distributed following the exponential probability density, independently of the degrees of freedom of the χ^2 variable considered (the logarithm of a variable that is uniformly distributed has an exponential probability density). Possible anomalies on the derivative fields are identified by looking at large values of $r_x(p)$, which correspond to large deviations of $\chi_x^2(p)$. In particular, the maximum of $r_x(p)$ can be computed:

$$r_x = \max_p \{r_x(p)\}. \quad (6.4)$$

Due to the intrinsic correlations on the field, the values of $r_x(p)$ for different pixels are correlated, which modifies the distribution of the maximum r_x , particularly at large scales, where the correlations dominates the field. For this reason, the probability distribution of r_x is calculated using a Monte Carlo method with 5000 simulations.

In figures 4 and 5, the upper and lower tail probabilities of r_x for each derivative are represented. Since a low variance in the derivative fields is observed, there is a preference

for small values of the lower tail probability, especially at the largest scales. For instance, at $R = 30^\circ$ the probability of having a value of r_ν lower than the observed value is about 3% in both SEVEM and SMICA data. The low variance is also manifested in η and ϵ , in which case the lower tail probability is below 3% for $R = 18^\circ$. Additionally in figures 4 and 5, in order to take into account this anomalous variance in the data, the statistics r_x are calculated using the observed covariance, instead of the covariance obtained from the theoretical fiducial model. In this case, the anisotropy introduced by the mask is also modelled using eq. (4.1), but replacing the matrix \mathbf{C} by the estimated covariance from the data. Once this correction for the low variance is done, the probabilities of r_η and r_ϵ are within the 2σ limits, while some values of r_ν and r_κ with upper tail probabilities $< 5\%$ are found.

The statistical deviation caused by the Cold Spot is observed at $R = 5^\circ$ as a decrement in the upper tail probability of r_κ . Since we are filtering the temperature with a Gaussian, the curvature map of the smoothed field is equivalently calculated by applying the Spherical Mexican Hat Wavelet (SMHW) [16], and therefore, the study of κ at different scales is equivalent to a multiscale analysis using the SMHW. In previous works [12] with the SMHW, the Cold Spot is characterized as the extreme value at 5° , which causes a deviation in the skewness at this scale. When the upper tail probability is computed using the theoretical fiducial model, the CS represents a relatively likely event with a probability of 6-8%, but if the low variance correction is done and the CS fluctuation is normalized by the observed variance instead of the theoretical one, this probability falls to $< 3\%$, as previously reported in [12] and [25]. Consequently, there is a statistical connection between the CS and the low variance anomaly, being a rare event having a large fluctuation as the CS in a field with such a low variance. Besides the curvature field, the combined analysis of ν and κ , where the correlation between them is taken into account, also presents a deviation at the scale of the CS and above. In particular, a fluctuation with similar significance to the CS (p -value about 1.2%) at the scale of $R \approx 10^\circ$ is observed. At this particular location in the sky, there is no extremum in the temperature field filtered with that scale, since the gradient is different than zero. However, at smaller scales, there is a hot spot at the same location. This peak and the Cold spot are the most prominent extrema in the κ field at the scale $R \approx 5^\circ$, which were previously identified in the SMHW analysis with a smaller probability in [25]. It is important to notice that these deviations may be caused by the low variance of the CMB temperature field at large scales, since when the analysis is performed comparing with the fiducial theoretical model, these fluctuations are less significant (see figure 4).

The locations of the maximum values of $r_x(p)$ for different scales are represented in figure 6. It is possible to see that, with the exception of the eccentricity ϵ , all the maxima lie in the Galactic southern hemisphere, and most of them in the particular quadrant coinciding with the CMB power asymmetry [26, 27]. It is important to remark that, in the case of the temperature ν , all the maxima for scales $R > 1^\circ$ are located in two of the largest spots in the sky, one cold and other hot. On the other hand, the gradient and the second order derivatives trace other large scale features (e.g. the Cold Spot, traced by the κ field). In the case of η and κ , the maximum deviation from the standard model are located near to the largest peaks observed in the temperature map, whereas deviations of the eccentricity tensor ϵ are spread along the field without any particular clustering around the largest structures. The excess of clustering of the ν maxima compared with high-order derivatives is caused by the particular scale dependence of the derivatives, which introduces extra ℓ factors, obtaining, in this way, less correlated extrema.

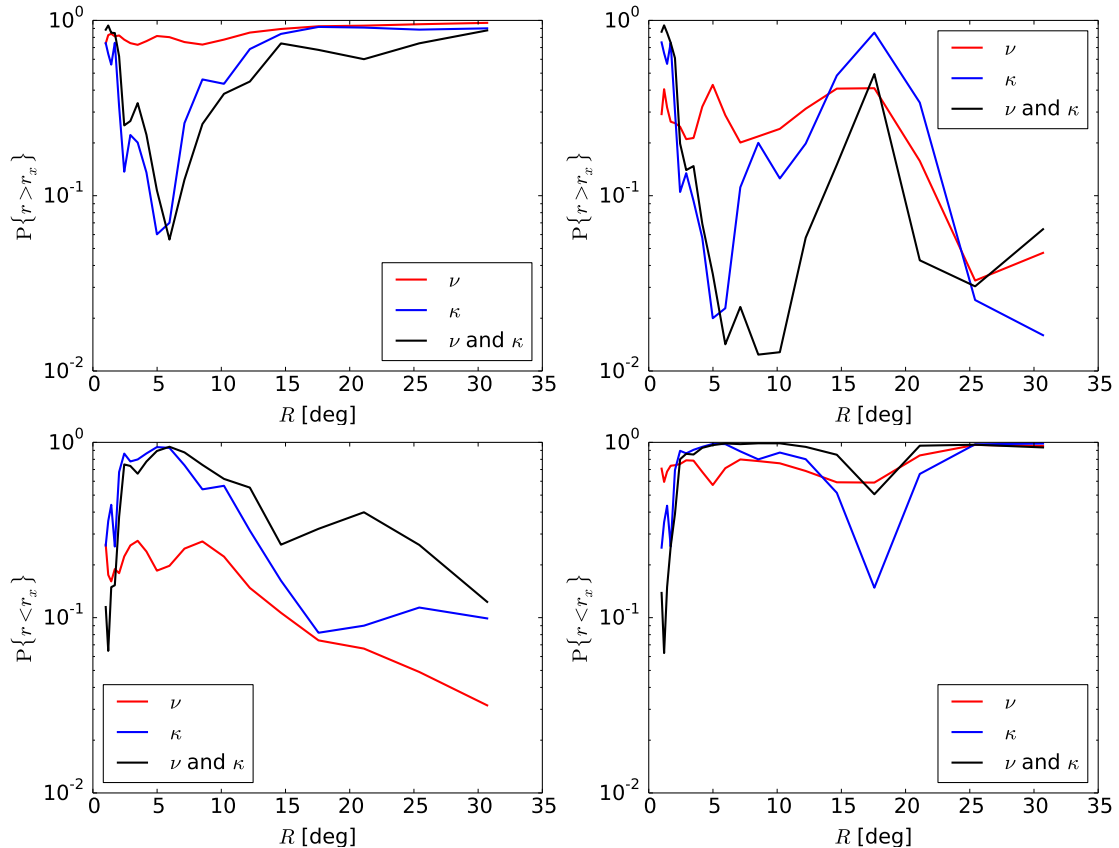


Figure 4. Upper tail probability (upper row) and lower tail probability (bottom row) of the maximum value r_x for the temperature, the curvature and the combination of both, obtained from the Planck SEVEM map. In the first column, the covariance is calculated from the theoretical fiducial model, whereas the probabilities in the second column are calculated using the covariance obtained from the data, in order to take into account the low variance.

7 Directional analysis

The gradient and the eccentricity tensor are spinorial quantities with non-zero spin, and therefore they have directional dependence which can be used to study alignment directions and the local isotropy of the field. In this section, an estimator of preferred directions in the sky for spinorial quantities is introduced. Given a particular point p on the sphere, we can construct all the geodesics connecting it with any other arbitrary point (see figure 7). This system of geodesics define a particular directional scheme associated to p , which can be used to project the spinorial field along this geodesics. The projected field is averaged using a particular weight function W , which depends on the size of the region around the point p where the isotropy is tested. If this process is repeated for all the possible points on the sphere, we get an estimator depending on the point p which define the anisotropy direction. For instance, in the case of the gradient, this estimator measures a possible excess of vectors pointing to a particular location on the sphere. This concept can be generalized for arbitrary spin quantities, maintaining a similar interpretation. In the case of the eccentricity tensor, which is a 2-spinor, this estimator indicates the existence of predominant directions where the

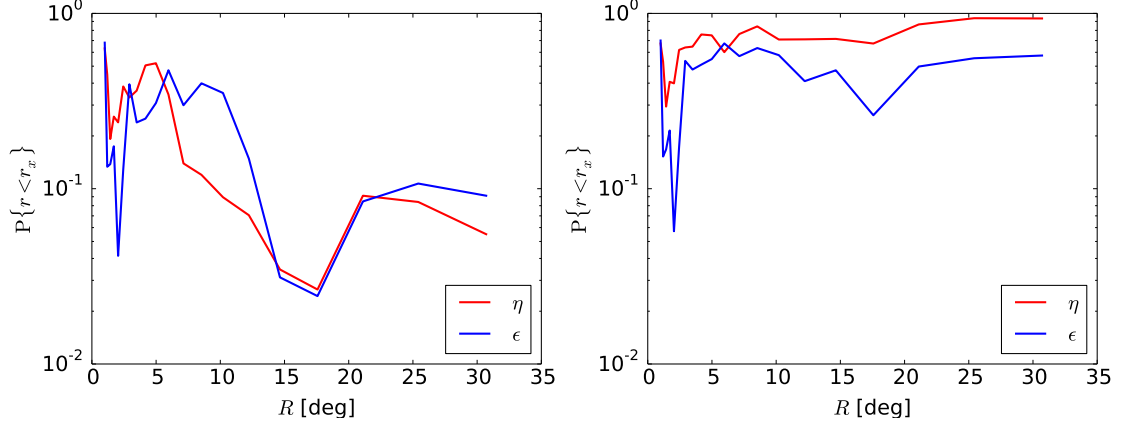


Figure 5. Lower tail probability of r_η and r_ϵ as a function of the scale, derived from the Planck SEVEM map. Whilst in the left figure the corresponding covariances are calculated from the theoretical fiducial model, the probabilities in the right figure are computed using the estimated covariance from the data.

local elongations of peaks are oriented. A similar analysis of the alignment of the eccentricity tensor (equivalent to the steerable wavelet basis formed by the second Gaussian derivatives) based on the intersection of great circles was applied to WMAP data in [18, 28].

Concretely, given a spinorial field ${}_s\zeta$ with spin s defined in the Galactic coordinates, the isotropy estimator associated to the direction defined by the point \mathbf{x} is:

$${}_s\bar{\zeta}(\mathbf{x}) = \int d^2\mathbf{y} W(\mathbf{x} \cdot \mathbf{y}) {}_s\zeta(\mathbf{y}) e^{is\alpha(\mathbf{x}, \mathbf{y})} , \quad (7.1)$$

where $\alpha(\mathbf{x}, \mathbf{y})$ is the angle between the Galactic north direction and the geodesic connecting the points \mathbf{x} and \mathbf{y} . The function W in this integral weights the contribution of the spinor at \mathbf{y} in the anisotropy direction defined by \mathbf{x} . In this way, the function W has information about the region around the point \mathbf{x} where the directional analysis performed. It is possible to see that the directional estimator ${}_s\bar{\zeta}(\mathbf{x})$ is a scalar field, which can be expanded in terms of the spin zero spherical harmonics. In general, this field is complex, and its real and imaginary parts correspond to the projection of different parity components of the spinor (see figure 7).

The estimator in eq. (7.1) can be written in the spherical harmonic space as:

$${}_s\bar{\zeta}(\mathbf{x}) = \sum_{l=|s|}^{\infty} \sum_{m=-l}^l D_\ell^s \sqrt{\frac{(\ell - |s|)!}{(\ell + |s|)!}} {}_s\zeta_{\ell m} Y_{\ell m}(\mathbf{x}) , \quad (7.2)$$

where ${}_s\zeta_{\ell m}$ are the spherical harmonics coefficient associated to the spinor ${}_s\zeta(\mathbf{x})$. The spin dependent quantities D_ℓ^s in eq. (7.2) are given by:

$$D_\ell^s = \sum_{\ell'=0}^{\infty} M_{\ell\ell'}^s W_{\ell'} , \quad (7.3)$$

where W_ℓ represents the coefficients of the filter W in eq. (7.1) in harmonic space and the

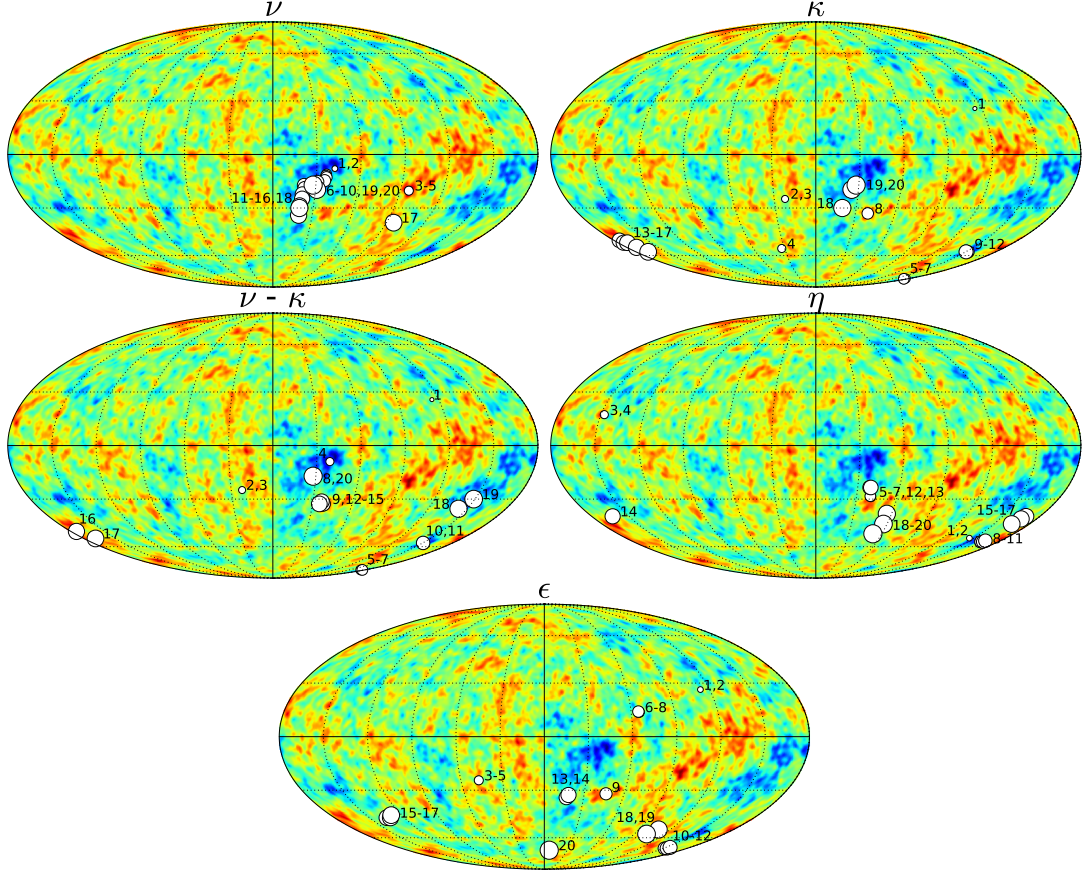


Figure 6. Locations of the maximum values of $r_x(p)$ for the derivatives fields at different scales. The locations are represented by white circles, whose size is proportional to the scale R considered. The field corresponding to each map is indicated in the title. The CMB temperature field corresponds to the Commander Planck map [21] smoothed by Gaussian with $R = 1^\circ$.

coupling matrix $M_{\ell\ell'}^s$ is given by

$$M_{\ell\ell'}^s = s(-1)^s (2\ell' + 1) \sqrt{\frac{(\ell + |s|)!}{(\ell - |s|)!}} \sum_{L=|\ell-\ell'|}^{\ell+\ell'} (2L + 1) \sqrt{\frac{(L - |s|)!}{(L + |s|)!}} \begin{pmatrix} \ell & \ell' & L \\ 0 & 0 & 0 \end{pmatrix} \begin{pmatrix} \ell & \ell' & L \\ s & 0 & -s \end{pmatrix} A_L^s. \quad (7.4)$$

In this expression, the numbers A_ℓ are related with integral of the spin-weighted spherical harmonics, which are defined in the Appendix A.

In the particular case of the gradient and the eccentricity tensor, it is possible to see that the estimator in eq. (7.1) can be obtained by filtering the temperature map with the filters D_ℓ^s :

$$\bar{\eta}(\mathbf{x}) = \sum_{\ell=1}^{\infty} \sum_{m=-\ell}^{\ell} D_\ell^1 a_{\ell m} Y_{\ell m}(\mathbf{x}), \quad (7.5a)$$

$$\bar{\epsilon}(\mathbf{x}) = \sum_{\ell=2}^{\infty} \sum_{m=-\ell}^{\ell} D_\ell^2 a_{\ell m} Y_{\ell m}(\mathbf{x}). \quad (7.5b)$$

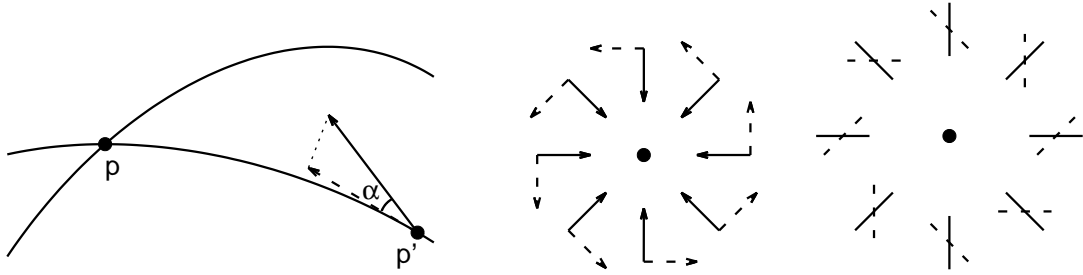


Figure 7. *Left:* projection of a vector field ($s = 1$) along the geodesic connecting p and p' as it is considered for the definition of the directional asymmetry estimator in eq. (7.1). *Right:* the two pictures represent the contribution of the spinor ${}_s\zeta$ field to the real and imaginary parts of ${}_s\bar{\zeta}(\mathbf{x})$. For simplicity, only the particular cases of $s = 1$ (vectors) and $s = 2$ (headless vectors) are depicted in the figure. The reference point \mathbf{x} used for the projection is indicated at the centre of a small flat patch of the sphere. The spinor components which have even parity (solid lines) contribute to the real part of ${}_s\bar{\zeta}$, whereas its imaginary part measures the contribution of the odd parity components (dashed lines). A change in the sign of ${}_s\bar{\zeta}$ can be seen as a rotation of π/s in the spinor field.

Notice that the directional estimators for the derivatives $\bar{\eta}(\mathbf{x})$ and $\bar{\epsilon}(\mathbf{x})$ are real scalar fields. Moreover, since they have a linear dependence on the temperature field, it is assumed that they are Gaussianly distributed, which simplify the calculations and the subsequent statistical analysis.

In this work, the weight function W used for averaging of the projected spinor in eq. (7.1) is assumed to be a disc centred at the point \mathbf{x}^1 . Particularly, discs with different radius are considered: 180° (full-sky average), 90° (one hemisphere) and 45° . The resulting filters D_ℓ^s for these three cases are represented in figure 8, for $s = 1$ and $s = 2$. The asymmetry in the multipoles with different parity, which is more evident in the filters with the largest averaging window, is a consequence of the transformation rules of the spinors under the rotation group. For instance, when a s -spinor is projected and averaged over the full sphere, the multipoles with parity different from s vanish because the field ${}_s\bar{\zeta}(\mathbf{x})$ has well-defined parity given by $(-1)^s$. More precisely, in this particular case, the value of ${}_s\bar{\zeta}$ at the point \mathbf{x} and at its antipode $-\mathbf{x}$ are related by a rotation of π radians, which introduces a factor -1 depending on the parity of the spinor (odd for the vector η and even for 2-spinors ϵ).

Within this formalism, the points on the sphere which present higher directional asymmetry in the derivatives correspond to extrema in the scalar fields $\bar{\eta}(\mathbf{x})$ and $\bar{\epsilon}(\mathbf{x})$, which, in particular, are a maximum or a minimum depending on whether the spinor tends to be aligned or anti-aligned with the direction given by \mathbf{x} . From this point of the study, these extrema are calculated and characterized in the same way as the analysis performed in Section 6, and with the same considerations for the mask derived in Section 4. The results are shown in figure 9, where we represent the p -value of the extrema in $\bar{\eta}$ and $\bar{\epsilon}$ observed in the data as a function of the scale R , as well as their corresponding location on the CMB field. The same three cases represented in figure 8 for the weight function are considered in the analysis. Whilst

¹In the harmonic space, the weight function W corresponding to a disc with radius θ is given by

$$W_\ell(\mu) = \begin{cases} -\sqrt{\frac{1+\mu}{1-\mu}} \frac{P_\ell^1(\mu)}{\ell(\ell+1)}, & \ell \neq 0 \\ 1, & \ell = 0 \end{cases},$$

where $\mu = \cos \theta$ and $P_\ell^1(\mu)$ is the associated Legendre polynomial with $m = 1$.

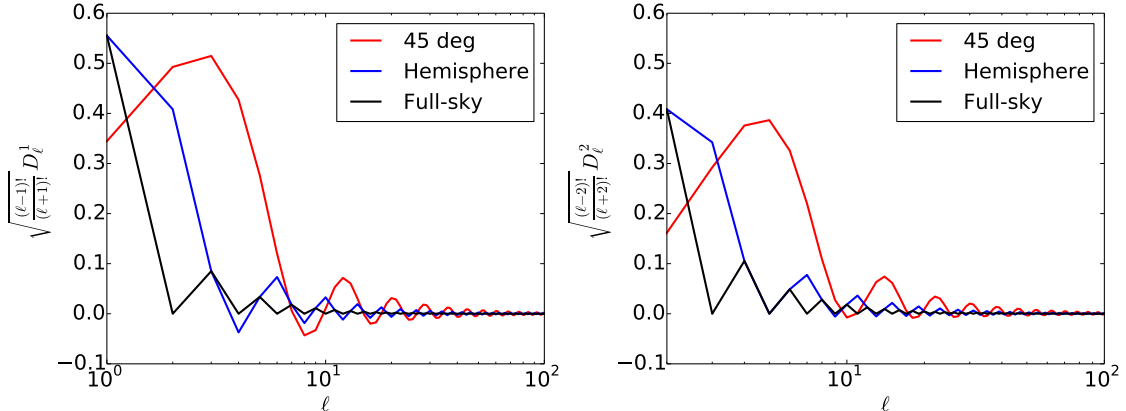


Figure 8. Filters D_ℓ^s for $s = 1$ (left) and $s = 2$ (right) used in the analysis of the directionality of spinors. Different curves correspond to different averaged area in the estimator.

the gradient is compatible with the standard model prediction, the eccentricity tensor has a preferred directionality when the spinor is averaged over an hemisphere. The probability of this deviation is only 0.2% for $R = 4^\circ$ in the SEVEM map, whereas this value increases up to 0.9% for the SMICA data. The corresponding anisotropic direction is located near the Galactic plane on one of the largest peaks of the CMB (see figure 9). However, notice that the main contribution to this deviation comes from a strip between 45° and 90° from the centre of this structure, since the estimator $\bar{\epsilon}$ for the 45° averaging is within the standard model limits.

8 Conclusions

In this work, the CMB temperature field is analysed by calculating its derivatives up to second order at different scales. One of the problems is that the incomplete sky (due to the masking of the Galactic emission and the point sources) causes a wrong determination of the derivatives at the border of the mask. In addition, other systematics appear when a convolution is applied to the masked data, since the filtering introduces a smearing of the mask border which is proportional to the filter scale. Therefore, in a multiscale analysis of the derivative fields, the handling of the mask is important in order to have a correct characterization of the derivatives. Due to the fact that the mask breaks the statistical isotropy of the field, the covariance of the fields depends on the pixel location, following the geometry given by the particular mask considered. The calculation of the pixel covariance is achieved in Section 4 by doing Monte Carlo simulations in an efficient way in order to reduce the simulation errors. For this purpose, the covariance at a given pixel is expressed as a linear transformation of the theoretical pixel-independent covariance, using a Cholesky-like decomposition. Following this procedure, we have that the temperature ν and the local curvature κ at a given pixel are correlated in a way determined by the theoretical fiducial model and the mask geometry. Besides, the components of the spinorial derivatives (the gradient and the eccentricity tensor), which are independent in an isotropic field, are correlated as a consequence of the incomplete sky.

Once the covariances between the different derivatives components have been determined at each pixel, an estimator of the theoretical full-sky covariances is proposed in Section 5, which generalizes the standard maximum likelihood estimator for full-sky data. A multiscale

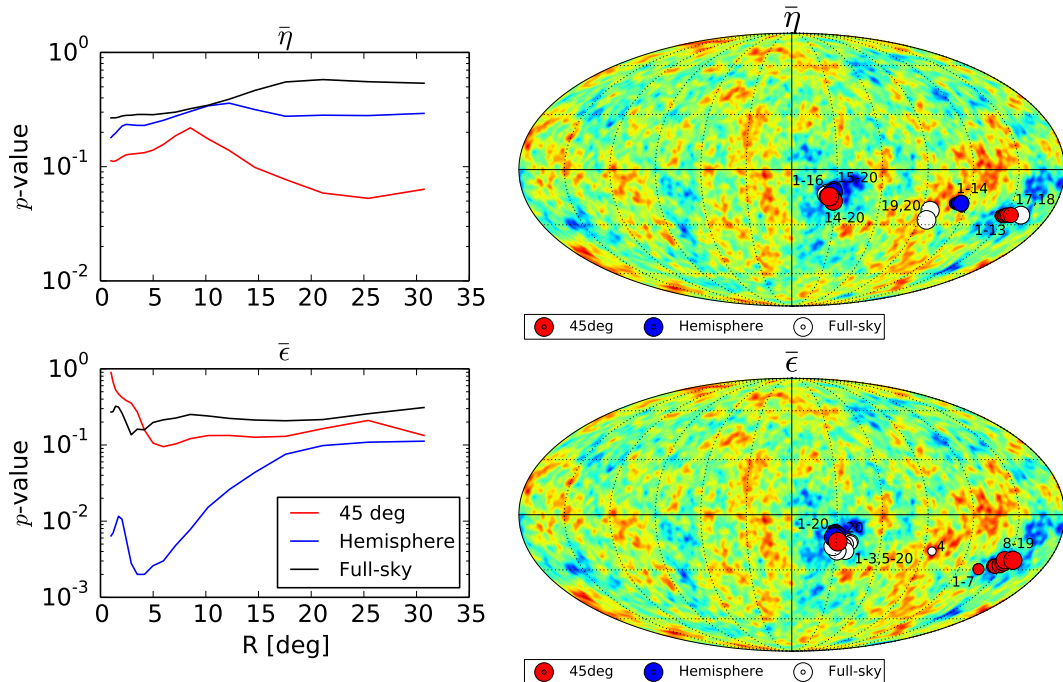


Figure 9. Directional analysis of the spinors η and ϵ using the three cases considered: full-sky, hemispherical and 45° averages. *Left:* the probabilities of finding a value of $\bar{\eta}$ (upper figure) and $\bar{\epsilon}$ (lower figure) as extreme as the maximum observed in the data for different scales. *Right:* the locations of these maxima on the CMB map are indicated with circles whose size is proportional to the scale R . The results presented in this figure are obtained from the Planck SEVEM map.

analysis is performed by calculating these covariances at different scales, finding that there is a systematic low variance preference at large scales in all the derivatives. Regarding the off-diagonal terms, an unusual low correlation between ν and κ is found when it is compared with its theoretical prediction. But, on the other hand, this effect disappears when the correlation term is normalized by the respective measured variances, indicating that the low correlation is directly related to the anomalous low variance.

Moreover, the isotropy of the field can be tested by looking at the variance of the gradient and the eccentricity tensor. If there is no preferred directions on the sky, the variances of each spinorial component must be the same, and the correlation between them should vanish. By comparing these assumptions as a function of the scale, no deviation from the isotropy is found in the CMB temperature. The statistical properties of the spinor components depend on the particular local system of reference used in their description, and therefore, this result is associated to the z axis of the standard Galactic coordinates. A more general analysis varying the azimuthal direction has to be performed in order to conclude that the derivatives are statistically isotropic.

The possible departure of the data from the standard model is quantified by looking at the deviation of the extreme values of the derivatives fields. The procedure consists in comparing the measured value of the derivative with the pixel covariance calculated in Section 6 using a χ^2 test. The deviations of the extreme values are quantified as the tail probability of finding that value in one realization. In this analysis, the observed low variance in the data

has an important role in the determination of this quantity, which causes that the extrema have particularly small values. In order to correct by this effect, pixel covariances which takes into account the mask geometry as well as the observed low variances of the derivative fields are introduced. Repeating the analysis with these modified covariances, the anomaly in the values of the extrema disappears in all the derivative fields, with the exception of κ , where deviations associated to the Cold Spot [12] and other large scale fluctuations are observed. In addition, a deviation at the scale $R = 10^\circ$ is highlighted in the combined analysis of the ν and κ whose p -value is comparable with the Cold Spot. The spatial location of the extrema is concentrated in the southern ecliptic hemisphere, a region which appear to be anomalous in other estimators of the statistical isotropy, as the dipole modulation [3]. It is possible to conclude from these results that the significance of these anomalies in the CMB temperature at large scales may be related of the low variance of the field. When these deviations are referred to the variance calculated from the theoretical model instead of the ones obtained from the data, the compatibility of the deviations increase to a probability of 6%.

Finally, in Section 7, an estimator of the local isotropy of the field based on the geodesic projection is developed for spinorial quantities. The mathematical formalism can be reduced to the application of a given kernel to the spherical harmonic coefficients, which is a function of the particular spin of the quantity considered. This directional analysis depends on the sky area used for averaging the projected spinor, which allows an analysis of isotropy at different scales. Since we are interested in the large scales, we consider three cases in our study: full-sky, one hemisphere and 45° averaged areas. As in the previous section, deviations from the standard model are characterized by the directions of maximum anisotropy. The results indicate that these directions correspond to the largest structures observed in the CMB temperature. In particular, it is observed a deviation whose p -value is ≈ 0.2 - 0.9% which is centred in one of the largest peaks near the Galactic plane. In a future work, this analysis of the isotropy of the CMB based on spinorial quantities will be generalized to the polarization spinor.

A Integrals of the spin-weighted spherical harmonics

The spatial average of the spin-weighted spherical harmonics are given by:

$$\frac{1}{4\pi} \int d^2\mathbf{x} {}_s Y_{\ell m}(\mathbf{x}) = s \sqrt{\frac{2\ell+1}{4\pi}} \sqrt{\frac{(\ell-|s|)!}{(\ell+|s|)!}} A_\ell^s \delta_{m0}, \quad (\text{A.1})$$

where the coefficients A_ℓ^s satisfy the relation $A_\ell^{-s} = A_\ell^s$, and they are defined only for $\ell \geq |s|$. In particular, in the case of $s = 1, 2$ we have

$$A_\ell^1 = \begin{cases} \frac{1}{4^{\ell+1}} \left(\frac{\ell+1}{2} \right)^2 \frac{\ell+1}{\ell} \frac{\pi}{2}, & \ell \text{ odd} \\ 0, & \ell \text{ even} \end{cases}, \quad (\text{A.2a})$$

$$A_\ell^2 = \begin{cases} 0, & \ell \text{ odd} \\ 1, & \ell \text{ even, } \ell \neq 0 \end{cases}. \quad (\text{A.2b})$$

The coefficients A_ℓ^1 can be easily calculated by using the following recurrence relation:

$$A_{\ell+2}^1 = \frac{\ell(\ell+2)}{(\ell+3)(\ell+1)} A_\ell^1, \quad (\text{A.3})$$

with initial values $A_0^1 = 0$ and $A_1^1 = 1/2$.

Acknowledgments

Partial financial support from the Spanish Ministerio de Economía y Competitividad Projects AYA2012-39475-C02-01 and Consolider-Ingenio 2010 CSD2010-00064 is acknowledged.

References

- [1] Planck Collaboration, P. A. R. Ade, N. Aghanim, M. Arnaud, M. Ashdown, J. Aumont, C. Baccigalupi, A. J. Banday, R. B. Barreiro, J. G. Bartlett, and et al., *Planck 2015 results. XIII. Cosmological parameters*, A&A **594** (Sept., 2016) A13, [[arXiv:1502.01589](#)].
- [2] C. Gordon, *Broken Isotropy from a Linear Modulation of the Primordial Perturbations*, ApJ **656** (Feb., 2007) 636–640, [[astro-ph/0607423](#)].
- [3] J. Hoftuft, H. K. Eriksen, A. J. Banday, K. M. Górski, F. K. Hansen, and P. B. Lilje, *Increasing Evidence for Hemispherical Power Asymmetry in the Five-Year WMAP Data*, ApJ **699** (July, 2009) 985–989, [[arXiv:0903.1229](#)].
- [4] K. Land and J. Magueijo, *Is the Universe odd?*, Phys. Rev. D **72** (Nov., 2005) 101302, [[astro-ph/0507289](#)].
- [5] J. Kim and P. Naselsky, *Anomalous parity asymmetry of WMAP 7-year power spectrum data at low multipoles: Is it cosmological or systematics?*, Phys. Rev. D **82** (Sept., 2010) 063002, [[arXiv:1002.0148](#)].
- [6] A. Gruppuso, F. Finelli, P. Natoli, F. Paci, P. Cabella, A. de Rosa, and N. Mandolesi, *New constraints on parity symmetry from a re-analysis of the WMAP-7 low-resolution power spectra*, MNRAS **411** (Mar., 2011) 1445–1452, [[arXiv:1006.1979](#)].
- [7] C. J. Copi, D. Huterer, D. J. Schwarz, and G. D. Starkman, *Large-scale alignments from WMAP and Planck*, MNRAS **449** (June, 2015) 3458–3470, [[arXiv:1311.4562](#)].
- [8] C. Monteserín, R. B. Barreiro, P. Vielva, E. Martínez-González, M. P. Hobson, and A. N. Lasenby, *A low cosmic microwave background variance in the Wilkinson Microwave Anisotropy Probe data*, MNRAS **387** (June, 2008) 209–219, [[arXiv:0706.4289](#)].
- [9] C. L. Bennett, M. Halpern, G. Hinshaw, N. Jarosik, A. Kogut, M. Limon, S. S. Meyer, L. Page, D. N. Spergel, G. S. Tucker, E. Wollack, E. L. Wright, C. Barnes, M. R. Greason, R. S. Hill, E. Komatsu, M. R. Nolta, N. Odegard, H. V. Peiris, L. Verde, and J. L. Weiland, *First-Year Wilkinson Microwave Anisotropy Probe (WMAP) Observations: Preliminary Maps and Basic Results*, ApJS **148** (Sept., 2003) 1–27, [[astro-ph/0302207](#)].
- [10] C. J. Copi, D. Huterer, D. J. Schwarz, and G. D. Starkman, *Lack of large-angle TT correlations persists in WMAP and Planck*, MNRAS **451** (Aug., 2015) 2978–2985, [[arXiv:1310.3831](#)].
- [11] P. Vielva, E. Martínez-González, R. B. Barreiro, J. L. Sanz, and L. Cayón, *Detection of Non-Gaussianity in the Wilkinson Microwave Anisotropy Probe First-Year Data Using Spherical Wavelets*, ApJ **609** (July, 2004) 22–34, [[astro-ph/0310273](#)].
- [12] M. Cruz, E. Martínez-González, P. Vielva, and L. Cayón, *Detection of a non-Gaussian spot in WMAP*, MNRAS **356** (Jan., 2005) 29–40, [[astro-ph/0405341](#)].
- [13] M. Zaldarriaga and U. Seljak, *Reconstructing projected matter density power spectrum from cosmic microwave background*, Phys. Rev. D **59** (June, 1999) 123507, [[astro-ph/9810257](#)].
- [14] B. Rathaus and E. D. Kovetz, *The CMB derivatives of Planck’s beam asymmetry*, MNRAS **443** (Sept., 2014) 750–754, [[arXiv:1405.1609](#)].
- [15] A. Marcos-Caballero et al., *Local properties of the large-scale peaks of the CMB temperature*, .

- [16] E. Martínez-González, J. E. Gallegos, F. Argüeso, L. Cayón, and J. L. Sanz, *The performance of spherical wavelets to detect non-Gaussianity in the cosmic microwave background sky*, MNRAS **336** (Oct., 2002) 22–32, [[astro-ph/0111284](#)].
- [17] Y. Wiaux, L. Jacques, and P. Vanderghelynst, *Correspondence Principle between Spherical and Euclidean Wavelets*, ApJ **632** (Oct., 2005) 15–28, [[astro-ph/0502486](#)].
- [18] P. Vielva, Y. Wiaux, E. Martínez-González, and P. Vanderghelynst, *Steerable wavelet analysis of CMB structures alignment*, New A Rev. **50** (Dec., 2006) 880–888, [[astro-ph/0609147](#)].
- [19] J. D. McEwen, B. Leistedt, M. Büttner, H. V. Peiris, and Y. Wiaux, *Directional spin wavelets on the sphere*, ArXiv e-prints (Sept., 2015) [[arXiv:1509.06749](#)].
- [20] A. Marcos-Caballero, R. Fernández-Cobos, E. Martínez-González, and P. Vielva, *The shape of CMB temperature and polarization peaks on the sphere*, J. Cosmology Astropart. Phys. **4** (Apr., 2016) 058, [[arXiv:1512.07412](#)].
- [21] Planck Collaboration, R. Adam, P. A. R. Ade, N. Aghanim, M. Arnaud, M. Ashdown, J. Aumont, C. Baccigalupi, A. J. Banday, R. B. Barreiro, and et al., *Planck 2015 results. IX. Diffuse component separation: CMB maps*, A&A **594** (Aug., 2016) A9, [[arXiv:1502.05956](#)].
- [22] K. M. Górski, E. Hivon, A. J. Banday, B. D. Wandelt, F. K. Hansen, M. Reinecke, and M. Bartelmann, *HEALPix: A Framework for High-Resolution Discretization and Fast Analysis of Data Distributed on the Sphere*, ApJ **622** (Apr., 2005) 759–771, [[astro-ph/0409513](#)].
- [23] M. Cruz, P. Vielva, E. Martínez-González, and R. B. Barreiro, *Anomalous variance in the WMAP data and Galactic foreground residuals*, MNRAS **412** (Apr., 2011) 2383–2390, [[arXiv:1005.1264](#)].
- [24] A. Gruppuso, P. Natoli, F. Paci, F. Finelli, D. Molinari, A. De Rosa, and N. Mandolesi, *Low variance at large scales of WMAP 9 year data*, J. Cosmology Astropart. Phys. **7** (July, 2013) 047, [[arXiv:1304.5493](#)].
- [25] Planck Collaboration, P. A. R. Ade, N. Aghanim, Y. Akrami, P. K. Aluri, M. Arnaud, M. Ashdown, J. Aumont, C. Baccigalupi, A. J. Banday, and et al., *Planck 2015 results. XVI. Isotropy and statistics of the CMB*, ArXiv e-prints (June, 2015) [[arXiv:1506.07135](#)].
- [26] H. K. Eriksen, F. K. Hansen, A. J. Banday, K. M. Górski, and P. B. Lilje, *Asymmetries in the Cosmic Microwave Background Anisotropy Field*, ApJ **605** (Apr., 2004) 14–20, [[astro-ph/0307507](#)].
- [27] F. K. Hansen, A. J. Banday, K. M. Górski, H. K. Eriksen, and P. B. Lilje, *Power Asymmetry in Cosmic Microwave Background Fluctuations from Full Sky to Sub-Degree Scales: Is the Universe Isotropic?*, ApJ **704** (Oct., 2009) 1448–1458, [[arXiv:0812.3795](#)].
- [28] Y. Wiaux, P. Vielva, E. Martínez-González, and P. Vanderghelynst, *Global Universe Anisotropy Probed by the Alignment of Structures in the Cosmic Microwave Background*, Physical Review Letters **96** (Apr., 2006) 151303, [[astro-ph/0603367](#)].